Article

The Effects of Ultrasound Treatment of Graphite on the Reversibility of the (De)Intercalation of an Anion from Aqueous Electrolyte Solution

Ghulam Abbas [1,2], Zahid Ali Zafar [2,3], Farjana J. Sonia [1], Karel Knížek [3], Jana Houdková [3], Petr Jiříček [3], Martin Kalbáč [1], Jiří Červenka [3] and Otakar Frank [1,*]

[1] J. Heyrovsky Institute of Physical Chemistry, Czech Academy of Sciences, Dolejskova 2155/3, 183 23 Prague, Czech Republic

[2] Department of Physical Chemistry and Macromolecular Chemistry, Faculty of Science, Charles University in Prague, Hlavova 2030, 128 43 Prague, Czech Republic

[3] FZU—Institute of Physics of the Czech Academy of Sciences, Cukrovarnicka 10/112, 162 00 Prague, Czech Republic

* Correspondence: otakar.frank@jh-inst.cas.cz

Abstract: Low cycling stability is one of the most crucial issues in rechargeable batteries. Herein, we study the effects of a simple ultrasound treatment of graphite for the reversible (de)intercalation of a ClO_4^- anion from a 2.4 M $Al(ClO_4)_3$ aqueous solution. We demonstrate that the ultrasound-treated graphite offers the improved reversibility of the ClO_4^- anion (de)intercalation compared with the untreated samples. The ex situ and in situ Raman spectroelectrochemistry and X-ray diffraction analysis of the ultrasound-treated materials shows no change in the interlayer spacing, a mild increase in the stacking order, and a large increase in the amount of defects in the lattice accompanied by a decrease in the lateral crystallite size. The smaller flakes of the ultrasonicated natural graphite facilitate the improved reversibility of the ClO_4^- anion electrochemical (de)intercalation and a more stable electrochemical performance with a cycle life of over 300 cycles.

1. Introduction

Overwhelming energy demand has propelled paramount interest in discovering the best ways to store energy in an environmentally friendly and sustainable manner [1]. For the development of more efficient and stable energy storage technologies, it is vital to explore different possible electrochemical charge storage mechanisms [2]. Graphite is one of the most studied electrode materials for batteries and supercapacitors, and has been extensively used in many lithium-ion, metal-ion, and nonmetal-ion energy storage devices [3,4]. The advantages of graphite are its high abundance, low cost, and versatility. Graphite allows the formation of many different types of graphite intercalation compounds (GICs) using both cations and anions [5,6]. For this reason, graphite is one of the most explored electrode materials in dual-ion batteries (DIBs).

DIBs are the trending contender in energy storage systems because they offer a wide variety of viable intercalation chemistries. Graphite-based electrodes are also favorable for DIBs because of the mechanical integrity of GICs. Graphite can accommodate even large ions and provide high cutoff voltages (e.g., 2.0–5.2 V vs. K/K^+ or 2.4–3.7 V vs. Al/Al^{3+}) and specific capacities (50–300 mAh g^{-1}) in organic and ionic liquid electrolytes [7]. GICs can be formed using metal cations, such as Li^+, Na^+, K^+, Zn^{2+}, Al^{3+}, and anions such as bis(trifluoromethanesulfonyl) imide $TFSI^-$, hexafluorophosphate PF_6^-, tetrafluoroborate BF_4^-, tetrachloroaluminate $AlCl_4^-$, and perchlorate ClO_4^- [8–16]. Even though graphite-based DIBs based on ionic liquid and organic electrolytes are promising in terms of stable

and reversible electrochemical performance, they have demerit points, such as flammability, high cost, environmental issues, or unsuitability for an open-air environment. These issues severely hinder their applicability across a wide variety of technology fields [17,18].

Aqueous electrolytes can potentially overcome the issues of organic and ionic liquid electrolytes in DIBs due to their inherent nonflammability, high ionic conductivity, and easy-to-handle nature in an open-air environment [19,20]. However, aqueous electrolytes suffer from small electrochemical potential windows of hydrogen and oxygen evolution reactions (~1.23 V) [21]. Highly concentrated aqueous electrolytes have recently enabled enlarging the electrochemical potential window by suppressing free water and reducing electrolyte decomposition [22]. Increased salt concentration in aqueous electrolytes has also enabled researchers to obtain lower-stage GICs and improve the reversibility of ionic (de)intercalation [23].

One of the highest electrochemical stabilities has been reported in highly concentrated $Al(ClO_4)_3$ and $Zn(ClO_4)_2$ aqueous electrolytes that offer an electrochemical window in the range of 3–4 V and the facile intercalation of the ClO_4^- anion in graphite [14,23]. However, the cycling stability and reversible ionic de(intercalation) in graphite during the discharge process are still key issues in ClO_4^--based electrolytes, limiting the cycling stability of perchlorate-based aqueous DIBs [14].

Over the years, researchers have investigated several different approaches for improving the reversibility of graphite intercalation in aqueous electrolytes [24–26]. Ultrasound treatment has changed the structural properties of graphite by inducing defects in the lattice structure and reducing its crystallite size [24–26]. The impact of the crystallite domain size (L_a) and degree of graphitization (g) on anion intercalation in graphite has been reported by Heckmann et al. [27], and also in our previous publication [28]. It has been found that a smaller crystallite domain size enhances ionic transport kinetics, which in turn improves the reversibility during the electrochemical (dis)charge process [29]. Generally, the reversibility of the intercalation process and kinetics at the electrode surface can be monitored by cyclic voltammetry (CV). However, to gain deeper insights into electrochemical ionic intercalation and to understand its correlation with the incurred structural modifications, various in situ studies featuring techniques such as X-ray diffraction (XRD), transmission electron microscopy (TEM), Raman spectroscopy, and X-ray photoelectron spectroscopy (XPS) are required [30,31]. Ostwald et al. performed in situ XPS to investigate the surface evolution of a graphite electrode material during the intercalation process in a Li-ion battery [32]. However, due to depth limitations, in situ XPS can only provide information about the first few nanometers from the surface of the material. TEM can provide atomically resolved pictures of the insertion/extraction process of the reactive ion [33], but the experiments are extremely demanding and cannot be routinely performed. Therefore, in situ Raman spectroelectrochemistry (SEC) and operando XRD are the most prominent tools that have been utilized to explore structural changes during the ion storage mechanism in detail [34,35]. Operando XRD reveals the lattice changes (contraction/expansion) in bulk during the electrochemical ionic intercalation process [36–39]. The operando XRD can be complemented by more surface-sensitive in situ Raman SEC, to provide information from the first tens to hundreds of nanometers depending on the studied material. It can also provide information about the reversibility of the charge/discharge process and the disorder induced in the material [23,28].

In this study, we report the effects of the mild ultrasound treatment of graphite on the reversibility of the (de)intercalation of the ClO_4^- anion using a 2.4 M $Al(ClO_4)_3$ aqueous solution. The intercalation process is characterized by electrochemistry (galvanostatic charge/discharge and CV) and by various in situ and ex situ techniques, including Raman spectroscopy, SEC, XRD, and XPS. The obtained results provide insight into the ClO_4^- anion intercalation mechanism in graphite, demonstrating a positive correlation between the (de)intercalation reversibility and the decrease in the lateral crystallite size by the ultrasound treatment.

2. Material and Methods

2.1. Material Preparation

A total of 200 mg of natural graphite (NG) (Nacional de Grafite, Ltda, Itapecerica, Brazil) was added into 60 mL of N-methyl-2-pyrrolidone (NMP) (Roth, Karlsruhe, Germany, ≥99.8% purity) solvent and ultrasonicated (Elmasonic P 00037510, 30 kHz, Singen, Germany) for 3 h. The micro flakes of NG were separated by centrifugation at 2500 rpm (Frontier Centrifuge FC5706, Parsippany, NJ, USA), collected, washed by ethanol, and dried under vacuum at 80 °C for 12 h. The ultrasonicated highly oriented pyrolytic graphite (HOPG) (NT-MDT, Moscow, Russia) was prepared using the same method. The pristine NG sample is further referred to as "NG" and the ultrasonicated NG and HOPG samples are referred to as "US-NG" and "US-HOPG".

2.2. Electrode Preparation

The graphite electrodes were prepared by casting a slurry onto a current collector of polytetrafluoroethylene (PTFE)-treated hydrophobic carbon paper of 150–200 μm thickness (120 Toray Carbon paper, Fuel Cell Store, College Station, TX, USA). The slurry was prepared by manually mixing the US-NG with conducting carbon black (Super-P, Imerys, Paris, France), polyvinylidene difluoride (PVDF) (Kynar® HSV 1800, Arkema, Colombes, France) as a binder, and NMP (75:15:10 wt. ratio) in a mortar. The as-prepared electrodes were dried at 80 °C under vacuum in an oven for 12 h prior to electrochemical testing.

2.3. Electrolyte Preparation

The 2.4 M $Al(ClO_4)_3$ aqueous electrolyte solution was prepared by dissolving 29.24 g of $Al(ClO_4)_3.9H_2O$ (Alfa Aesar, Haverhill, MA, USA) in 10 mL of deionized (DI) water. The solution was stirred for 30 min at room temperature to obtain a clear solution.

2.4. Electrochemical Cycling

The galvanostatic charge/discharge cycling was performed from −0.08 to 1.55 V (vs. Ag/AgCl) in a three-electrode standard electrochemical cell by using an Ag/AgCl pseudo-reference electrode and a platinum wire as a counter electrode in the concentrated $Al(ClO_4)_3$ aqueous electrolyte. A μ-Autolab type III workstation (Metrohm, Herisau, Switzerland) was used for electrochemical measurements. Cyclic voltammetry (CV) tests were conducted in the potential window of −0.08 to 1.58 V (vs. Ag/AgCl) at various sweep rates from 1 to 9 mVs^{-1}. For the ex situ characterizations, all the samples were washed in DI water and dried in a vacuum oven at 70 °C for 2 h prior to the measurements. The electrodes were discharged to −0.08 V and charged till 1.55 V (vs. Ag/AgCl), and subsequently referred to as "discharged" and "charged", respectively, and those without any electrochemical activity were referred to as "fresh".

2.5. Material Characterization

Scanning electron microscopy (SEM) images were obtained using a TESCAN MAIA3 microscope (Brno, Czech Republic). X-ray diffraction (XRD) was performed on Bruker D8 (Bruker, Karlsruhe, Germany) with Cu Kα radiation (λ = 1.5418 Å). The X-ray diffractogram was recorded at 0.01° per step with a slit width of 0.6 mm in order to improve the accuracy of the XRD measurement. A Horiba Lab-RAM HR (Lille, France) equipped with an Olympus microscope, a 633 nm He-Ne excitation laser operated at 1 mW power by 600 lines/mm grating (1.8 cm^{-1} point-to-point spectral resolution), and a 100× long working distance objective, was used to record the Raman spectra.

The in situ Raman spectroelectrochemistry measurements were performed in a home-made cell, using the same setup with the potential held for about 1000 s for each step. The prepared samples served as the working electrodes, a chlorinated Ag wire was used as the reference electrode, and Pt was used as the counter electrode; Autolab PGSTAT30 (Metrohm, Herisau, Switzerland) was used for the Raman-SEC measurement. The operando XRD analysis was performed using the same setup and conditions as the ex situ analyses. The

X-rays penetrate through the KAPTON tape (Tob Xiamen, Xiamen, China) window from the top. The XRD was connected with a battery tester (Neware, Hong Kong, China) for galvanostatic charge/discharge in a two-electrode setup at 20 μAg^{-1} current density. All the measurements were recorded at 2θ in the range of 10–60° with a step of 0.02° using a *Lynxeye XE-T* detector and applying a voltage of 40 kV and 30 mA current.

The ex situ XPS of the fresh, charged, and discharged samples were performed using an AXIS Supra photoelectron spectrometer (Kratos Analytical Ltd., Manchester, UK) with an Al Kα monochromatic energy source. The XPS analysis of US-NG material was performed by ADES 400 (VG Scientific, London, UK) with an Al Kα monochromatic energy source. The spectra were recorded after sputter-etching the samples with Ar$^+$ ion clusters (the number of Ar atoms in the cluster was 1000) of 5 keV energy for 10 min. The elemental composition was calculated from the high-resolution core level spectra with respect to the relative sensitivity factor. The determined uncertainties in concentration correspond to the deviation in the measured atomic % of the elements, and were calculated by ESCApe 1.4.0 software (Kratos analytical Ltd., Manchester, UK).

3. Results and Discussion

3.1. Structural Properties of Graphite and Electrochemical (De)Intercalation of $ClO_4{}^-$ Anion

The SEM images of the US-NG (Figure S1c,d in the Supplementary Materials) show more disjointed and crumpled structures in comparison to NG (Figure S1a,b). The ultrasound treatment of graphite leads to a partial disintegration of the bulk crystallites to flakes of varying thickness and lateral dimensions. Figure 1a displays the XRD patterns of the NG and US-NG. The resulting structural parameters are summarized in Table 1. The XRD (002) peaks of the NG and US-NG were recorded at 2θ of 26.53(8)° and 26.54(4)°, corresponding to the interlayer spacing (d_{002}) of 3.35(6) Å and 3.35(5) Å, respectively. For comparison, the XRD (002) peak of the US-HOPG (Figure S2a) recorded at 2θ of 26.53(1)° corresponds to the interlayer spacing of 3.35(6) Å. The degree of graphitization (g), calculated on the basis of d_{002} (see Supplementary Materials Equation (S1)) was also found to be very similar, and close to perfectly crystalline graphite for NG, US-NG, (Table 1) and US-HOPG (Table S1). The coherent domain size (L_c) for the stacking along the c-axis for the hexagonal graphitic structure was calculated using the Scherrer equation (Supplementary Materials Equation (S2)) [40]. The calculated L_c was 52.20 nm to 84.89 nm for NG and US-NG, respectively (Table 1), and 97.50 nm for the US-HOPG (Table S1).

Figure 1b shows the Raman spectra of NG and US-NG. The Raman G band at 1583 cm^{-1} and the 2D band at 2500–2700 cm^{-1} are the typical Raman signatures of graphite [41]. In addition, disorder-related D and D′ bands at 1350 cm^{-1} and 1620 cm^{-1}, respectively, can be seen in all the spectra. Importantly, the ultrasonication results in higher intensities of the D and D′ bands, thereby pointing to a more defective crystalline structure (Figure 1b). The inter-defect distance (L_D), defect density (n_D) and lateral domain size (L_a) were calculated from the ratio of the D and G band intensities (I_D/I_G) by the equations as reported by Cancado et al. (Supplementary Materials Equations (S3)–(S5)) [42]. The calculated structural parameters are summarized in Table 1. The larger I_D/I_G ratio of the US-NG (I_D/I_G = 0.18) corresponds to lattice changes with a smaller inter-defect distance (L_D) of ~ 44 nm in comparison to the NG (I_D/I_G = 0.11, L_D ~ 51 nm). The other two structural parameters, defect density (n_D) and crystallite size (L_a), follow the same trend as L_D (Table 1). The US-HOPG (I_D/I_G = 0.04) (Figure S2b) shows smaller lattice changes with an L_D of ~84 nm (Table S1). L_a refers to the mean lateral crystallite size, an important parameter to describe the structural properties of the graphite. As can be seen from the data above, the ultrasonication treatment of NMP does not have a substantial influence on the interlayer spacing (and graphitization degree). However, the coherent domain size L_c of NG increases with the treatment. The increase in L_c might be caused by the relaxation of the carbon hexagons as the lateral dimensions of the graphitic planes become smaller. The ultrasound cleaves the layers at the weaker defective sites, which might have been imposing stress, thereby lowering the L_c in the pristine material. Similar behavior was observed for carbon fibers [43]. Moreover, the

increase in I_D/I_G after ultrasonication corresponds to more functional groups' decorated defects at the edges of graphite, which in turn provide more active sites and enhance the electrochemical activity [44]. The Raman spectra-derived parameters corroborate the data obtained by XRD, evidencing the increase in structural damage caused by the ultrasonication treatment which has, consequently, a substantial influence on electrochemical performance and will be discussed in detail in the following sections.
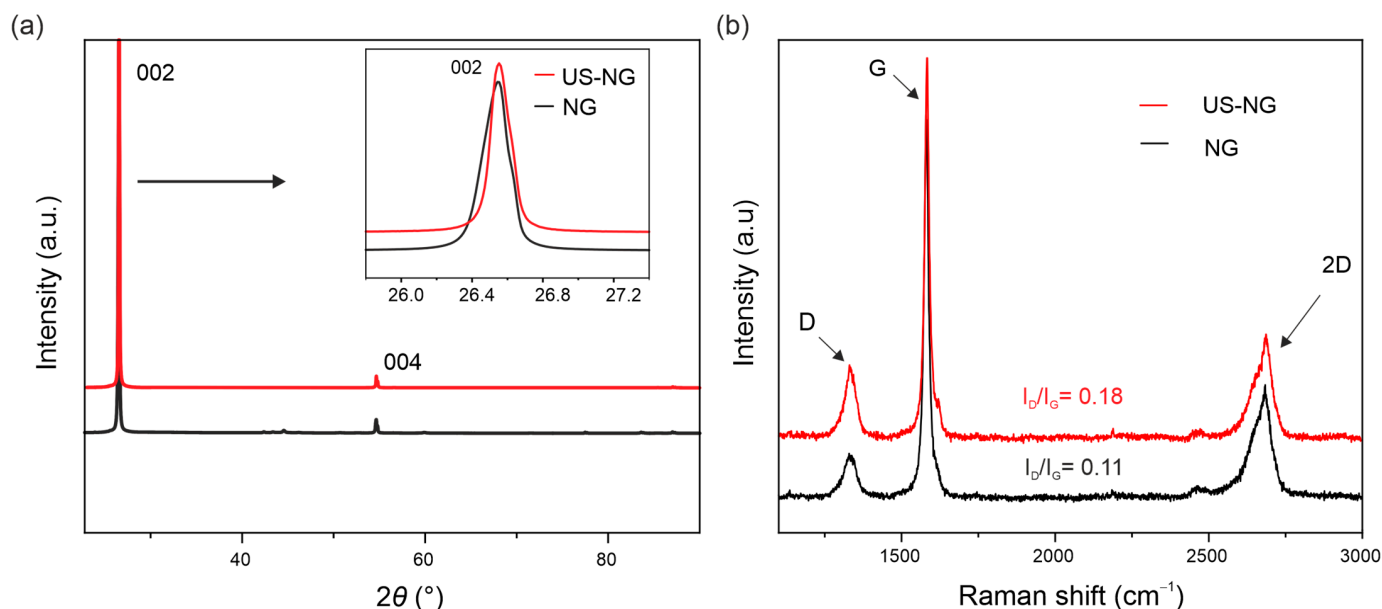

Figure 1. Structural characterization: (**a**) XRD and (**b**) Raman spectra of NG (black curves) and US-NG (red curves).

Table 1. Quantification of structural parameters of NG and US-NG from XRD and Raman spectroscopy.

Material	g (%)	L_c (nm)	L_D (nm)	n_D (cm^{-2})	L_a (nm)
NG	97.67	52.20	51.26 ± 0.14	$(12.33 \pm 0.27) \times 10^9$	350.29
US-NG	98.58	84.89	44.43 ± 0.02	$(20.20 \pm 0.11) \times 10^9$	214.07

The electrochemical characteristics of US-NG were studied in 2.4 M Al(ClO$_4$)$_3$ aqueous electrolyte concerning the (de)intercalation of the ClO$_4^-$ anion. Figure 2a shows the cyclic voltammograms (CVs) of NG and US-NG recorded at a sweep rate of 1 mVs^{-1}. The CVs show two redox peaks in both the cathodic and anodic regions. The electrochemical intercalation of the ClO$_4^-$ ions in the graphite is attributed to the two oxidation peaks at 1.43 V (O´$_A$) and 1.55 V (O$_A$) (~4.7 to 4.8 V vs. Li/Li$^+$) and the reduction peaks at 1.16 V (R´$_C$) and 1.35 V (R $_C$) [45,46]. The different multiple peaks during the intercalation/deintercalation of the anion into graphite correspond to the different staging mechanisms [47,48]. The visibleble plateaus at around 1.55 V during galvanostatic charge, and at 1.35 V and 1.16 V during the discharge of NG and US-NG (Figure 2b), correspond to the intercalation and (de)intercalation of ClO$_4^-$ ions, respectively, which is in line with the CV profile. Likewise, the CV of US-HOPG (Figure S3a) shows similar redox peaks (O$_A$, O´$_A$, R$_C$, and R´$_C$). The difference in the galvanostatic charge/discharge profile of NG and US-NG (Figure 2b) could be due to the relatively smaller lateral crystallite size of the US-NG compared to NG.
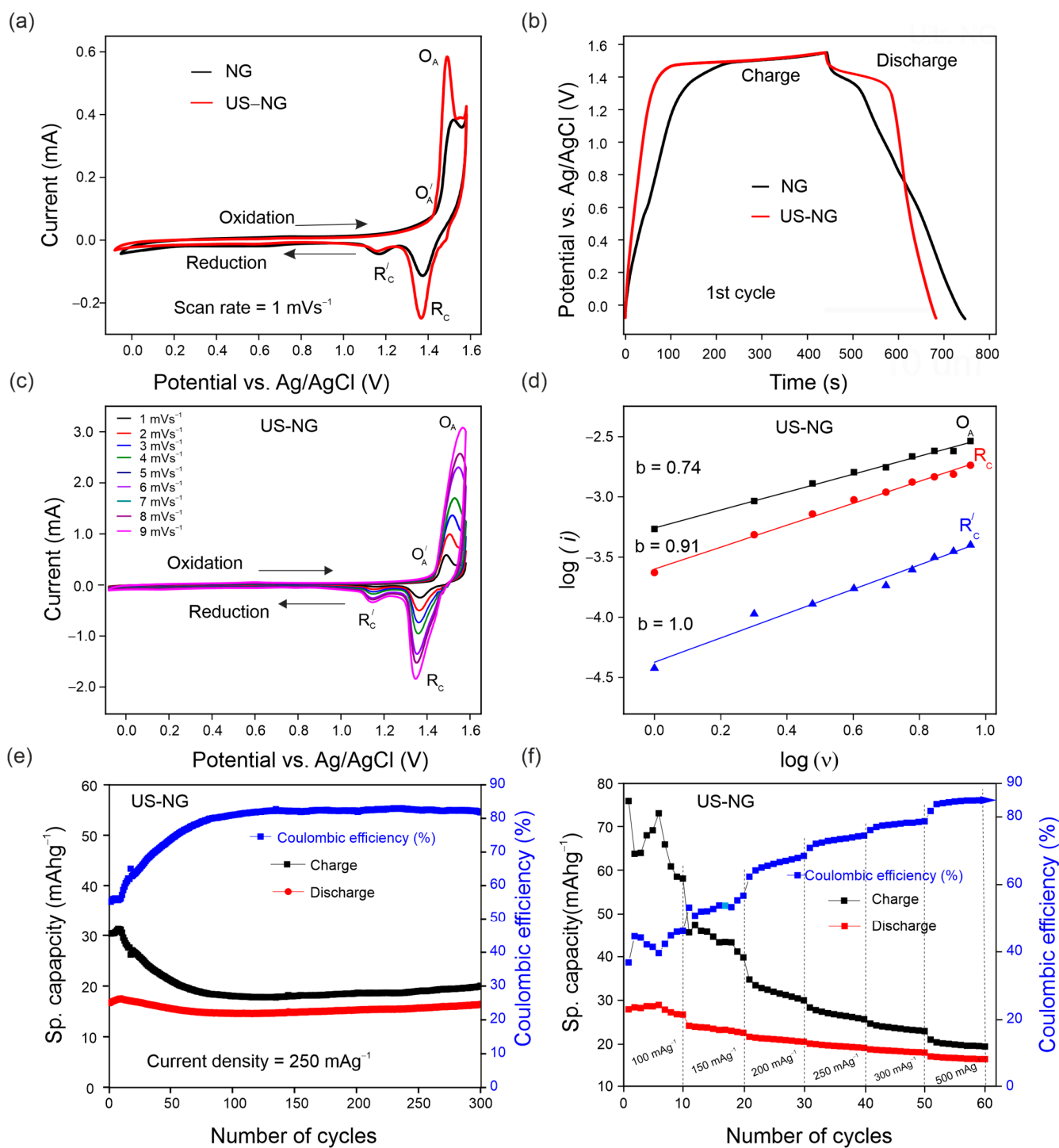
Figure 2. Electrochemical performance of US-NG using 2.4 M Al(ClO$_4$)$_3$ aqueous electrolyte solution: (**a**) CVs of NG and US-NG at 1 mVs^{-1}; (**b**) galvanostatic charge/discharge potential profile of NG and US-NG at a current density of 250 mAg^{-1} (1st cycle); (**c**) CVs of US-NG at different scan rates (1 to 9 mVs^{-1}); (**d**) electrochemical kinetic of log (*i*) vs. log (*ν*) at the redox peaks for US-NG; (**e**) galvanostatic cycling charge/discharge performance of US-NG obtained at a current density of 250 mAg^{-1}; (**f**) the rate capability of US-NG for specific capacities at various current densities ranging from 100 mAg^{-1} to 500 mAg^{-1} using 2.4 M Al(ClO$_4$)$_3$ aqueous electrolyte solution.

To reveal the nature of the electrochemical process of US-NG in detail, the analysis of CVs with varying scan rates (Figure 2c) can unbraid the contributions of diffusion and surface-controlled processes by using the power–law relationship of the peak current (i) and scan rate (v) (SI Equation (S6)) [49,50]. Figure 2d shows the CV kinetics of US-NG, where the fitted b values of 0.74 for the oxidation peak O_A and 0.91 for the reduction peak R_C indicate the contribution of both ionic diffusion and surface-controlled processes, while the b value of 1.0 for the R'_C reduction peak evidences the contribution of purely surface-controlled processes.

The galvanostatic charge/discharge cycling curves of US-NG were recorded in 2.4 M $Al(ClO_4)_3$ aqueous electrolyte at a current density of 250 mAg^{-1}. The US-NG shows a stable discharge capacity of ~18 $mAhg^{-1}$ for 300 cycles, with Coulombic efficiency larger than 80% (Figure 2e). The discharge capacity of ~18 $mAhg^{-1}$ for US-HOPG in 2.4 M $Al(ClO_4)_3$ aqueous electrolyte at a current density of 250 mAg^{-1} was also observed for 125 cycles, as shown in Figure S3c. A similar charge/discharge performance for graphitic electrode materials in both aqueous and non-aqueous electrolytes has been reported previously [23,39,51].

Ultrasound treatment leads to smaller crystallites (larger surface) and more active sites at the surface, which enhances electrochemical activity [52]. The smaller lateral crystallite size might have a substantial influence on the cyclic stability, as well as on the reversibility of the (de)intercalation of the ClO_4^- anion in US-NG. It is well known that defects are introduced into the lattice structure of graphite due to the attachment of functional groups during the ultrasound treatment in different solvents [53–55]. Skaltsas et al. reported that the ultrasonication of graphite in NMP induces the formation of defects accompanied by the increase in the concentration of the oxygenated species (COOH, COO) in the material [53]. Here, we observed the presence of the hydroxyl and carboxyl oxygen-containing functional groups attached to the graphitic carbon of US-NG by XPS analysis, as shown in Figure S4. We note that the analysis was performed after Ar^+ ion etching to minimize the potential influence of airborne contamination. The elemental analysis for US-NG is presented in Table S2. The oxygenated species at the graphite lattice could originate from the decomposition of NMP or surface oxidation during the ultrasound treatment [26]. The functional groups decorating the graphite surface could facilitate the large-size ions accessing the graphite interlayer galleries through surface adsorption during the electrochemical process [56–60]. Figure 2f displays the specific capacity of US-NG recorded at various current densities from 100 mAg^{-1} to 500 mAg^{-1}. It also shows a stable electrochemical performance with an increase in Coulombic efficiency at high current density (500 mAg^{-1}). Figure S3d shows the rate capability of US-HOPG from 100 mAg^{-1} to 500 mAg^{-1}.

3.2. In Situ Characterization

In order to obtain deeper insights on the ionic (de)intercalation into US-NG, in situ Raman SEC was performed. Figure 3a displays the Raman spectra of US-NG acquired in situ during the charge/discharge cycle. The G peak, being the most sensitive to the interaction of ions with the graphite planes, splits into two components. The low-frequency (~1584 cm^{-1}) G(i) mode and high-frequency (~1613 cm^{-1}) G(b) mode appear due to the formation of GICs with the anions inside the interlayer galleries [25,61,62]. The splitting of the G peak at 1.40 V (vs. Ag/AgCl) during the charging process, accompanied by a further intensity increase in the G(b) peak, corresponds to the gradual intercalation of the ClO_4^- ion in the interlayer spaces of graphite. The complete disappearance of the G(b) mode during the discharge process is attributed to a fully reversible deintercalation [63–65]. This observation is in line with the stable discharge capacity in the case of US-NG over long cycles, as shown in Figure 2e. In spite of the hysteresis in the G peak position during the charge/discharge cycle, Figure 3b shows that the graphite lattice is completely restored after the (de)intercalation of the ClO_4^- anion. Comparatively, during a galvanostatic discharge, in the case of untreated NG, the persistence of the G(b) mode during the discharge process

was attributed to the only partial reversibility of the (de)intercalation of the ClO_4^- anion, as shown in our previous publication [28].
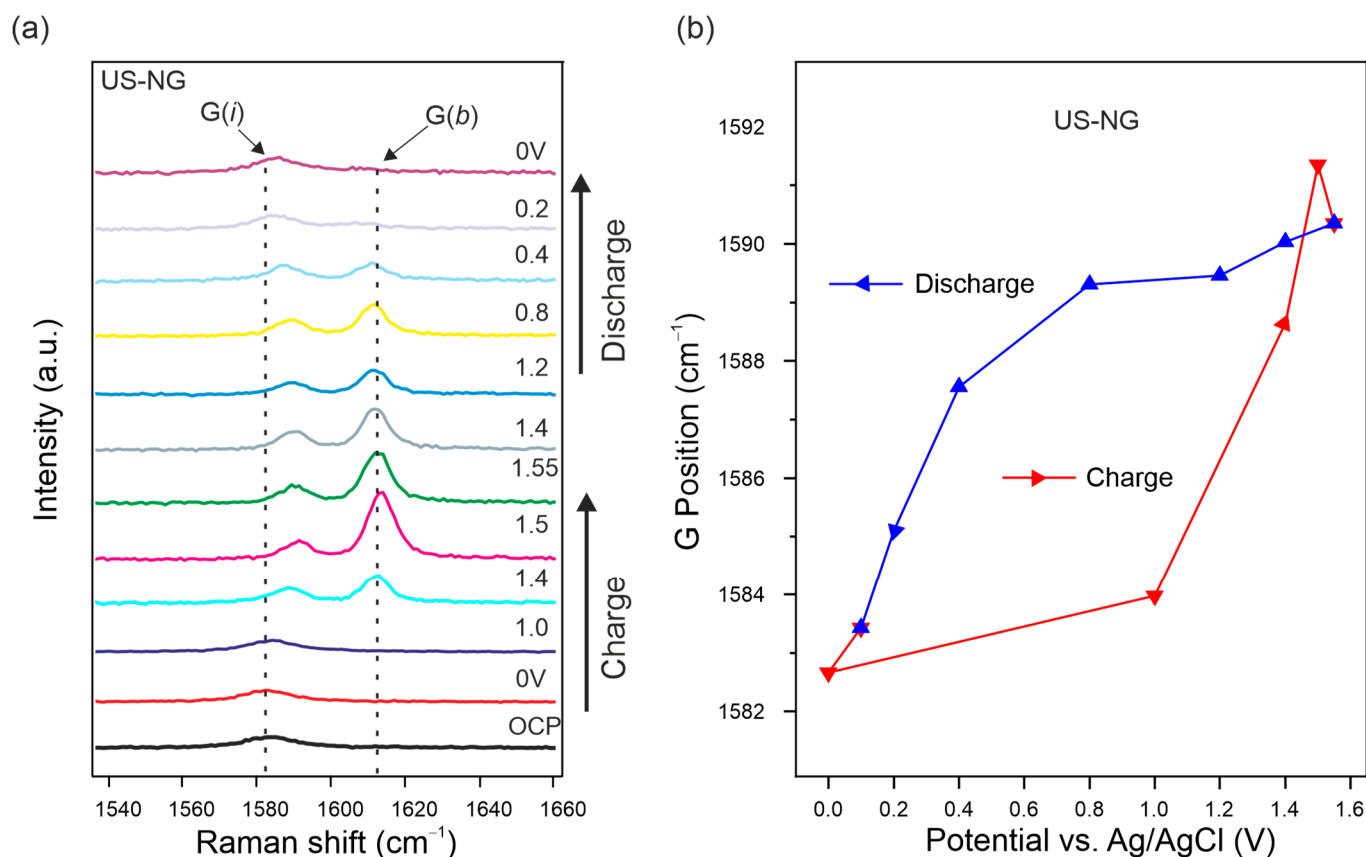

Figure 3. In situ Raman SEC of US-NG during charge/discharge cycle in 2.4 M $Al(ClO_4)_3$ aqueous electrolyte. (**a**) Evolution of the Raman spectra in the G peak spectral region. (**b**) Raman G peak position evolution fitted as one Lorentzian line shape. The applied potentials were held for 1000 s for each step.

Operando XRD proved to be an efficient tool to monitor the structural lattice modifications taking place alongside the GIC formation during the charge/discharge process [66,67]. Figure 4 shows the evolution of the (002) and (004) reflections of US-NG during one charge/discharge cycle. The characteristic graphitic (002) reflection broadens and splits during the charge process due to the intercalation of the ClO_4^- anion [23]. The emerged reflection has 2θ of ~25.5°, corresponding to d_{002} of ~3.49 Å. Analogous behavior can be observed in the (004) reflection. Decreases in broadening and intensity in the main reflections were observed upon charging, which also depicts the ionic intercalation into graphite. The peaks were fully recovered during the discharge process (Figure 4).
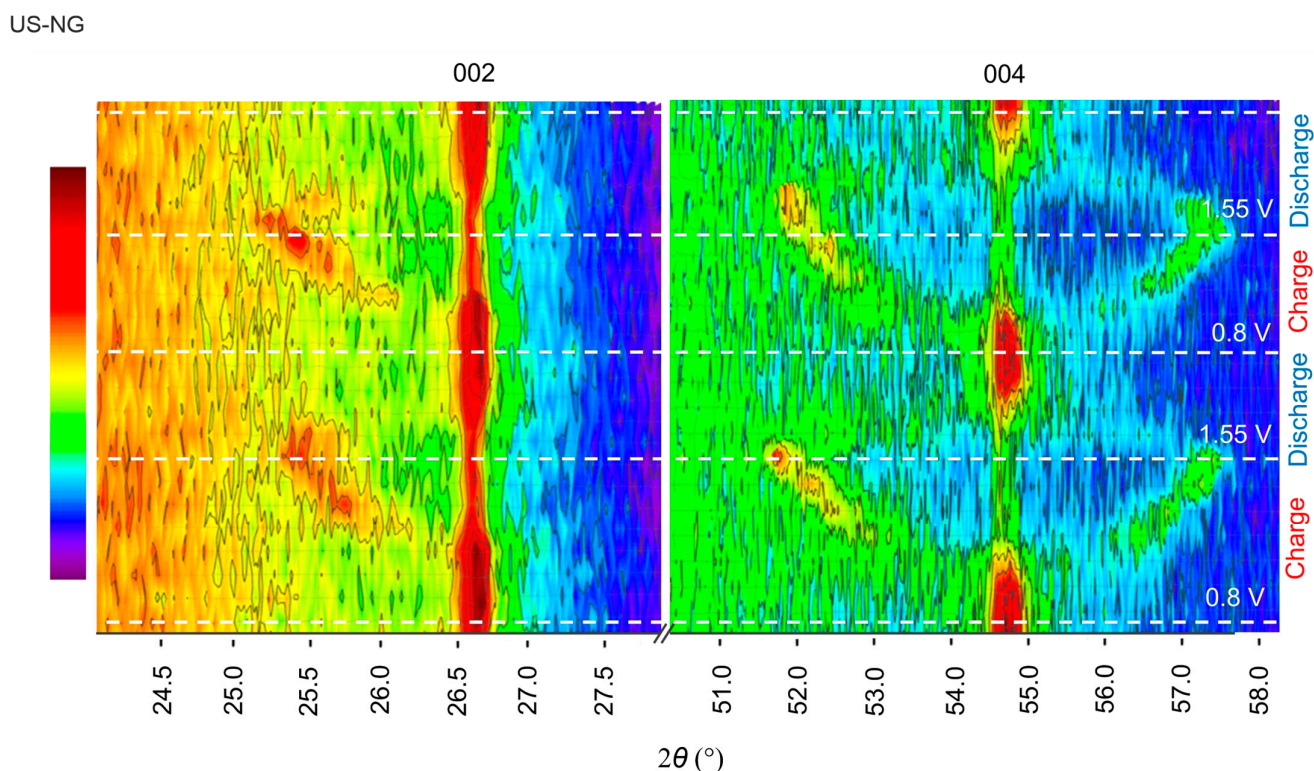
US-NG

Figure 4. Operando XRD analysis of US-NG during charge/discharge process in 2.4 M Al(ClO$_4$)$_3$ aqueous electrolyte solution.

3.3. Ex Situ Spectroscopic Characterization

To describe the (de)intercalation process in more detail, additional ex situ spectroscopic techniques, such as ex situ Raman spectroscopy and ex situ XPS, were performed on the fresh, charged, and discharged US-NG electrodes.

The ex situ Raman spectra of US-NG show an increase in the intensity ratio of the D to G peaks (I_D/I_G) during the charged state (0.31) in comparison to the discharged (0.24) and fresh (0.17) states (Figure S5a), illustrating the reversible structural changes during the intercalation of the ClO$_4^-$ anion [39]. Similarly, the ex situ Raman spectra of US-HOPG (Figure S5b) also show an increase in I_D/I_G ratio (0.17) during charging in comparison to the discharged (0.15) and fresh (0.03) states. The incomplete recovery of the small D peak intensity points to the partial irreversibility of the intercalation in US-HOPG.

The chemical composition of fresh, discharged, and charged US-NG electrode materials were analyzed by XPS (Figure 5). Figure 5a shows the survey XPS spectra of the electrodes, with the lines assigned to Cl, Al, O, C, and F labelled. The presence of F comes from the electrode binder [68]. Figure 5c,d shows the high-resolution Cl 2p core-level XPS spectra of US-NG during the charged/discharged state, demonstrating the presence of the two chemical states of Cl. The lower-energy component at ~200 eV corresponds to Cl covalently bonded to carbon atoms (C-Cl) [69]; the peaks at 201.9 eV and 200.1 eV belong to the 2p$_{1/2}$ and 2p$_{3/2}$ energy levels, respectively. The higher-energy state at ~208 eV corresponds to ClO$_4^-$. The peaks at 209.6 eV and 208.0 eV correspond to Cl 2p$_{1/2}$ and Cl 2p$_{3/2}$, respectively, attributed to the adsorbed ClO$_4^-$, possibly originating from the electrolyte presence at the surface of the electrode [70,71]. Cl 2p$_{1/2}$ and Cl 2p$_{3/2}$ at 208.0 eV and 206.4 eV, respectively, reveal the intercalated ClO$_4^-$ ion [14,72]. The elemental composition (Table S3) and selected ratios of the atoms or ions (Table 2) evidence that higher amounts of ClO$_4^-$ were present in the charged than in the discharged US-NG. Importantly, the ratio of intercalated/adsorbed ClO$_4^-$ was observed to be significantly higher for the charged state than for the discharged state (Figure 5c,d). We noted that an exact quantification of the intercalated/adsorbed ClO$_4^-$ is not possible due to the overlap of the spin-split

peaks at the binding energy of 208.0 eV (Cl $2p_{1/2}$ of the intercalated ClO_4^- and Cl $2p_{3/2}$ of the adsorbed ClO_4^-). Nevertheless, the amount of intercalated ClO_4^- is very low in the discharged state, also taking into account the very low Cl content (Table S3), which can explain the structural reversibility seen in Raman SEC and XRD. Figure 5b shows the Al 2p core level at 75.5 eV binding energy. The concentration of Al (Table S3) was observed to be higher for the charged US-NG electrodes, compared to the discharged one. Additionally, the Al to C ratio in the charged US-NG is higher than in the discharged US-NG (Table 2), which might correspond to the trapped electrolyte in the US-NG electrode.
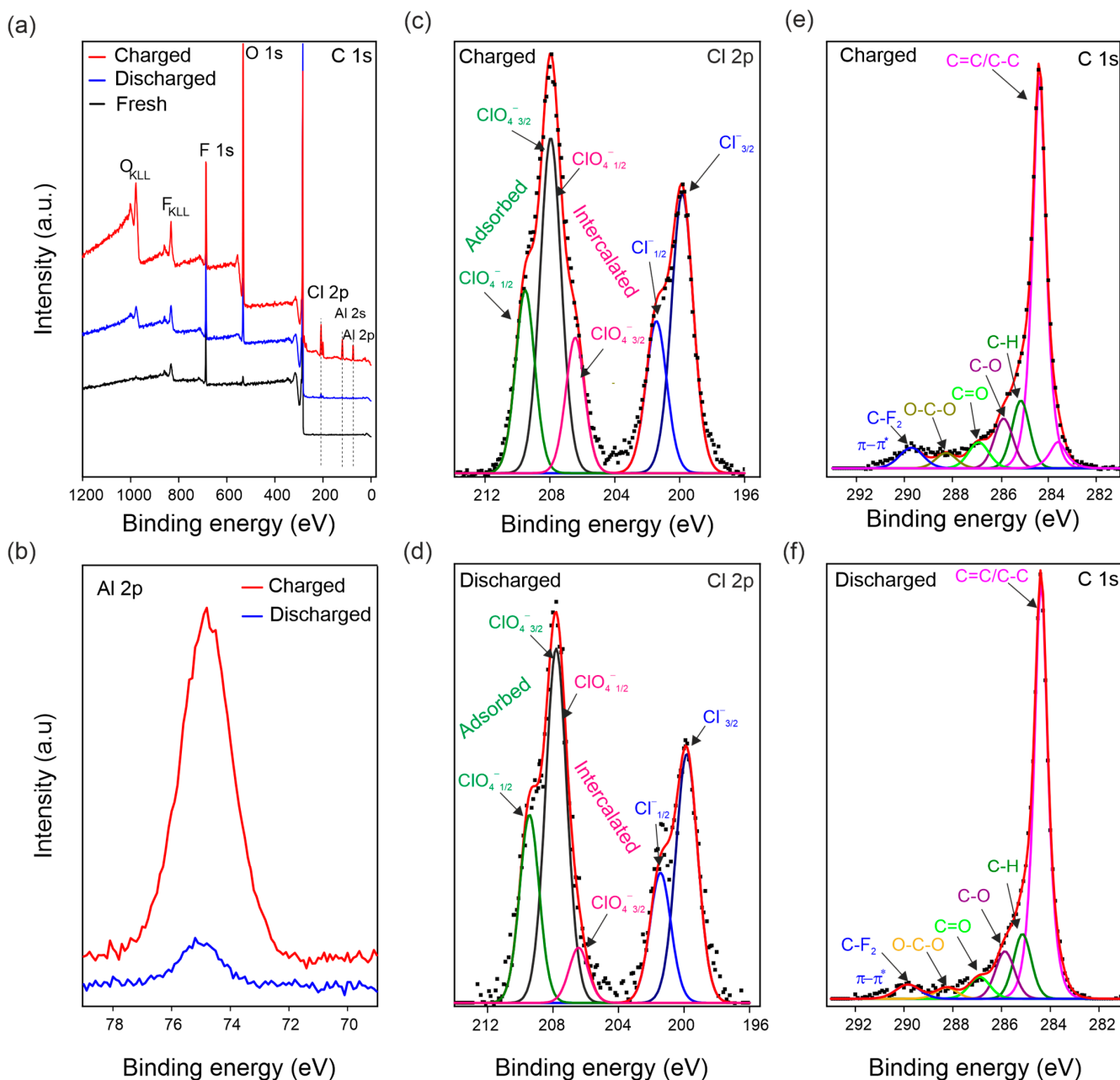

Figure 5. Ex situ XPS analysis of US-NG in fresh, charged, and discharged states using 2.4 M $Al(ClO_4)_3$ aqueous electrolyte solution. (**a**) Survey XPS spectrum; (**b**) high-resolution XPS spectra of the Al 2p core levels in the charged and discharged states; deconvoluted high-resolution XPS spectra of the Cl 2p core levels in the charged (**c**) and discharged states (**d**) (note, the Cl $2p_{1/2}$ of intercalated ClO_4^- and Cl $2p_{3/2}$ of adsorbed ClO_4^- overlap at 208.0 eV); deconvoluted high-resolution XPS spectra of the C 1s core levels in the charged (**e**) and discharged states (**f**).

Table 2. Concentration ratios of ClO_4^- and Cl and Al and C for US-NG derived from XPS.

Sample	US-NG	
	Charged	**Discharged**
Cl/C	0.059	0.010
ClO_4^-/C	0.335	0.080
Al/ClO_4^-	0.227	0.080
Al/C	0.076	0.010

4. Conclusions

The effect of the ultrasound treatment of natural and highly oriented pyrolytic graphite on the reversibility of electrochemical (de)intercalation of the ClO_4^- anion was studied in aqueous $Al(ClO_4)_3$ electrolyte solution. The ultrasonication of graphite in NMP induced the formation of defects accompanied by a reduction in its crystallite size, L_a. The smaller L_a of US-NG in comparison to pristine NG facilitated the easier escape of the large-size ions from the graphite interlayer galleries, thereby enhancing the reversibility and cyclic stability. The in situ Raman SEC and operando XRD of US-NG confirmed the reversibility of the structural changes in the graphite induced by the ClO_4^- intercalation, although a remaining signal of the intercalated ClO_4^- species was detected by ex situ XPS. The study shows that ultrasound treatment offers a practical approach for improving the reversibility of electrochemical intercalation processes in graphite, which can also help in designing novel functional graphite intercalation materials for energy storage systems.

Data Availability Statement: The data presented in this study are available on request from the corresponding author. The data are not publicly available due to IP protection revision of related studies.

Conflicts of Interest: The authors declare no conflict of interest.

References

1. Dunn, B.; Kamath, H.; Tarascon, J.M. Electrical energy storage for the grid: A battery of choices. *Science* **2011**, *334*, 928–935. [CrossRef] [PubMed]
2. Thackeray, M.M.; Wolverton, C.; Isaacs, E.D. Electrical energy storage for transportation—Approaching the limits of, and going beyond, lithium-ion batteries. *Energy Environ. Sci.* **2012**, *5*, 7854–7863. [CrossRef]

3. Rothermel, S.; Meister, P.; Schmuelling, G.; Fromm, O.; Meyer, H.W.; Nowak, S.; Winter, M.; Placke, T. Dual-graphite cells based on the reversible intercalation of bis(trifluoromethanesulfonyl)imide anions from an ionic liquid electrolyte. *Energy Environ. Sci.* **2014**, *7*, 3412–3423. [CrossRef]

4. Rodríguez-Pérez, I.A.; Zhang, L.; Wrogemann, J.M.; Driscoll, D.M.; Sushko, M.L.; Han, K.S.; Fulton, J.L.; Engelhard, M.H.; Balasubramanian, M.; Viswanathan, V.V.; et al. Enabling Natural Graphite in High-Voltage Aqueous Graphite ‖ Zn Metal Dual-Ion Batteries. *Adv. Energy Mater.* **2020**, *10*, 2001256. [CrossRef]

5. Inagaki, M. Applications of graphite intercalation compounds. *J. Mater. Res.* **1989**, *4*, 1560–1568. [CrossRef]

6. Dresselhaus, M.S.; Dresselhaus, G. Intercalation compounds of graphite. *Adv. Phys.* **2002**, *51*, 1–186. [CrossRef]

7. Ji, B.; Zhang, F.; Song, X.; Tang, Y. A Novel Potassium-Ion-Based Dual-Ion Battery. *Adv. Mater.* **2017**, *29*, 1700519. [CrossRef]

8. Rodríguez-Pérez, I.A.; Ji, X. Anion Hosting Cathodes in Dual-Ion Batteries. *ACS Energy Lett.* **2017**, *2*, 1762–1770. [CrossRef]

9. Placke, T.; Fromm, O.; Rothermel, S.; Schmuelling, G.; Meister, P.; Meyer, H.-W.; Passerini, S.; Winter, M. Electrochemical Intercalation of Bis(Trifluoromethanesulfonyl) Imide Anion into Various Graphites for Dual-Ion Cells. *ECS Trans.* **2013**, *50*, 59–68. [CrossRef]

10. Kondo, Y.; Miyahara, Y.; Fukutsuka, T.; Miyazaki, K.; Abe, T. Electrochemical intercalation of bis(fluorosulfonyl)amide anions into graphite from aqueous solutions. *Electrochem. Commun.* **2019**, *100*, 26–29. [CrossRef]

11. Zhu, D.; Wang, H. Hexafluorophosphate Anion Intercalation into Graphite Electrodes from Propylene Carbonate/Gamma-Butyrolactone Solutions. *Langmuir* **2021**, *37*, 10797–10805. [CrossRef] [PubMed]

12. Wang, Y.; Li, J.; Huang, Y.; Wang, H. Anion Storage Behavior of Graphite Electrodes in LiBF4/Sulfone/Ethyl Methyl Carbonate Solutions. *Langmuir* **2019**, *35*, 14804–14811. [CrossRef] [PubMed]

13. Lv, Z.; Han, M.; Sun, J.; Hou, L.; Chen, H.; Li, Y.; Lin, M.C. A high discharge voltage dual-ion rechargeable battery using pure (DMPI+)(AlCl4−) ionic liquid electrolyte. *J. Power Sources* **2019**, *418*, 233–240. [CrossRef]

14. Zafar, Z.A.; Abbas, G.; Knizek, K.; Silhavik, M.; Kumar, P.; Jiricek, P.; Houdková, J.; Frank, O.; Cervenka, J. Chaotropic anion based "water-in-salt" electrolyte realizes a high voltage Zn-graphite dual-ion battery. *J. Mater. Chem. A* **2022**, *10*, 2064–2074. [CrossRef]

15. Bordet, F.; Ahlbrecht, K.; Tübke, J.; Ufheil, J.; Hoes, T.; Oetken, M.; Holzapfel, M. Anion intercalation into graphite from a sodium-containing electrolyte. *Electrochim. Acta* **2015**, *174*, 1317–1323. [CrossRef]

16. Zhu, J.; Li, Y.; Yang, B.; Liu, L.; Li, J.; Yan, X.; He, D. A Dual Carbon-Based Potassium Dual Ion Battery with Robust Comprehensive Performance. *Small* **2018**, *14*, 1801836. [CrossRef]

17. Xu, K. Electrolytes and interphases in Li-ion batteries and beyond. *Chem. Rev.* **2014**, *114*, 11503–11618. [CrossRef]

18. Jiang, X.; Luo, L.; Zhong, F.; Feng, X.; Chen, W.; Ai, X.; Yang, H.; Cao, Y. Electrolytes for Dual-Carbon Batteries. *ChemElectroChem* **2019**, *6*, 2615–2629. [CrossRef]

19. Wang, P.; Chen, Z.; Wang, H.; Ji, Z.; Feng, Y.; Wang, J.; Liu, J.; Hu, M.; Fei, J.; Gan, W.; et al. A high-performance flexible aqueous Al ion rechargeable battery with long cycle life. *Energy Storage Mater.* **2020**, *25*, 426–435. [CrossRef]

20. Nandi, S.; Das, S.K. Realizing a Low-Cost and Sustainable Rechargeable Aqueous Aluminum-Metal Battery with Exfoliated Graphite Cathode. *ACS Sustain. Chem. Eng.* **2019**, *7*, 19839–19847. [CrossRef]

21. Liu, Z.; Huang, Y.; Huang, Y.; Yang, Q.; Li, X.; Huang, Z.; Zhi, C. Voltage issue of aqueous rechargeable metal-ion batteries. *Chem. Soc. Rev.* **2020**, *49*, 180–232. [CrossRef] [PubMed]

22. Liang, T.; Hou, R.; Dou, Q.; Zhang, H.; Yan, X. The Applications of Water-in-Salt Electrolytes in Electrochemical Energy Storage Devices. *Adv. Funct. Mater.* **2021**, *31*, 2006749. [CrossRef]

23. Zafar, Z.A.; Abbas, G.; Silhavik, M.; Knizek, K.; Kaman, O.; Sonia, F.J.; Kumar, P.; Jiricek, P.; Houdková, J.; Frank, O.; et al. Reversible anion intercalation into graphite from aluminum perchlorate "water-in-salt" electrolyte. *Electrochim. Acta* **2022**, *404*, 139754. [CrossRef]

24. Ng, K.L.; Malik, M.; Buch, E.; Glossmann, T.; Hintennach, A.; Azimi, G. A low-cost rechargeable aluminum/natural graphite battery utilizing urea-based ionic liquid analog. *Electrochim. Acta* **2019**, *327*, 135031. [CrossRef]

25. Liu, C.; Liu, Z.; Niu, H.; Wang, C.; Wang, Z.; Gao, B.; Liu, J.; Taylor, M. Preparation and in-situ Raman characterization of binder-free u-GF@CFC cathode for rechargeable aluminum-ion battery. *MethodsX* **2019**, *6*, 2374–2383. [CrossRef]

26. Kokai, F.; Sorin, R.; Chigusa, H.; Hanai, K.; Koshio, A.; Ishihara, M.; Koga, Y.; Hasegawa, M.; Imanishi, N.; Takeda, Y. Ultrasonication fabrication of high quality multilayer graphene flakes and their characterization as anodes for lithium ion batteries. *Diam. Relat. Mater.* **2012**, *29*, 63–68. [CrossRef]

27. Heckmann, A.; Fromm, O.; Rodehorst, U.; Münster, P.; Winter, M.; Placke, T. New insights into electrochemical anion intercalation into carbonaceous materials for dual-ion batteries: Impact of graphitization degree. *Carbon N. Y.* **2018**, *131*, 201–212. [CrossRef]

28. Abbas, G.; Sonia, F.J.; Zafar, Z.A.; Knížek, K.; Houdková, J.; Jiříček, P.; Bouša, M.; Plšek, J.; Kalbáč, M.; Červenka, J.; et al. Influence of structural properties on (de-)intercalation of ClO_4^- anion in graphite from concentrated aqueous electrolyte. *Carbon N. Y.* **2022**, *186*, 612–623. [CrossRef]

29. Kaewmala, S.; Limphirat, W.; Yordsri, V.; Kim, H.; Muhammad, S.; Yoon, W.S.; Srilomsak, S.; Limthongkul, P.; Meethong, N. Structural and Electrochemical Kinetic Properties of $0.5Li_2MnO_3 \cdot 0.5LiCoO_2$ Cathode Materials with Different Li_2MnO_3 Domain Sizes. *Sci. Rep.* **2019**, *9*, 427. [CrossRef]

30. Zou, J.; Sole, C.; Drewett, N.E.; Velický, M.; Hardwick, L.J. In Situ Study of Li Intercalation into Highly Crystalline Graphitic Flakes of Varying Thicknesses. *J. Phys. Chem. Lett.* **2016**, *7*, 4291–4296. [CrossRef]

31. Li, N.; Su, D. In-situ structural characterizations of electrochemical intercalation of graphite compounds. *Carbon Energy* **2019**, *1*, 200–218. [CrossRef]
32. Oswald, S.; Nikolowski, K.; Ehrenberg, H. Quasi in situ XPS investigations on intercalation mechanisms in Li-ion battery materials. *Anal. Bioanal. Chem.* **2009**, *393*, 1871–1877. [CrossRef] [PubMed]
33. Zhang, Y.; Lu, F.; Pan, L.; Xu, Y.; Yang, Y.; Bando, Y.; Golberg, D.; Yao, J.; Wang, X. Improved cycling stability of NiS2 cathodes through designing a "kiwano" hollow structure. *J. Mater. Chem. A* **2018**, *6*, 11978–11984. [CrossRef]
34. Fan, H.; Qi, L.; Wang, H. Intercalation Behavior of Hexafluorophosphate into Graphite Electrode from Propylene/Ethylmethyl Carbonates. *J. Electrochem. Soc.* **2017**, *164*, A2262–A2267. [CrossRef]
35. Wang, B.; Wang, Y.; Huang, Y.; Zhang, L.; Ma, S.; Wang, H. Hexafluorophosphate Intercalation into the Graphite Electrode from Mixed Cyclic Carbonates. *ACS Appl. Energy Mater.* **2021**, *4*, 5316–5325. [CrossRef]
36. Wang, D.Y.; Huang, S.K.; Liao, H.J.; Chen, Y.M.; Wang, S.W.; Kao, Y.T.; An, J.Y.; Lee, Y.C.; Chuang, C.H.; Huang, Y.C.; et al. Insights into dynamic molecular intercalation mechanism for Al[sbnd]C battery by operando synchrotron X-ray techniques. *Carbon N. Y.* **2019**, *146*, 528–534. [CrossRef]
37. Zhu, D.; Huang, Y.; Zhang, L.; Fan, H.; Wang, H. PF$_6$—Intercalation into Graphite Electrode from Gamma-butyrolactone/ethyl Methyl Carbonate. *J. Electrochem. Soc.* **2020**, *167*, 070513. [CrossRef]
38. Seel, J.A.; Dahn, J.R. Electrochemical Intercalation of PF$_6$ into Graphite. *J. Electrochem. Soc.* **2000**, *147*, 892. [CrossRef]
39. Gao, J.; Tian, S.; Qi, L.; Wang, H. Intercalation manners of perchlorate anion into graphite electrode from organic solutions. *Electrochim. Acta* **2015**, *176*, 22–27. [CrossRef]
40. Akikubo, K.; Kurahashi, T.; Kawaguchi, S.; Tachibana, M. Thermal expansion measurements of nano-graphite using high-temperature X-ray diffraction. *Carbon N. Y.* **2020**, *169*, 307–311. [CrossRef]
41. Ferrari, A.C.; Meyer, J.C.; Scardaci, V.; Casiraghi, C.; Lazzeri, M.; Mauri, F.; Piscanec, S.; Jiang, D.; Novoselov, K.S.; Roth, S.; et al. Raman spectrum of graphene and graphene layers. *Phys. Rev. Lett.* **2006**, *97*, 18740. [CrossRef] [PubMed]
42. Cançado, L.G.; Jorio, A.; Ferreira, E.H.M.; Stavale, F.; Achete, C.A.; Capaz, R.B.; Moutinho, M.V.O.; Lombardo, A.; Kulmala, T.S.; Ferrari, A.C. Quantifying defects in graphene via Raman spectroscopy at different excitation energies. *Nano Lett.* **2011**, *11*, 3190–3196. [CrossRef] [PubMed]
43. Lim, S.; Yoon, S.H.; Mochida, I.; Chi, J.H. Surface modification of carbon nanofiber with high degree of graphitization. *J. Phys. Chem. B* **2004**, *108*, 1533–1536. [CrossRef]
44. Wu, C.; Cheng, Q.; Wu, K. Electrochemical Functionalization of N -Methyl-2-pyrrolidone-Exfoliated Graphene Nanosheets as Highly Sensitive Analytical Platform for Phenols. *Anal. Chem.* **2015**, *87*, 3294–3299. [CrossRef] [PubMed]
45. Liu, T.; Zhu, C.; Kou, T.; Worsley, M.A.; Qian, F.; Condes, C.; Duoss, E.B.; Spadaccini, C.M.; Li, Y. Ion Intercalation Induced Capacitance Improvement for Graphene-Based Supercapacitor Electrodes. *ChemNanoMat* **2016**, *2*, 635–641. [CrossRef]
46. Bu, X.; Su, L.; Dou, Q.; Lei, S.; Yan, X. A low-cost "water-in-salt" electrolyte for a 2.3 V high-rate carbon-based supercapacitor. *J. Mater. Chem. A* **2019**, *7*, 7541–7547. [CrossRef]
47. Schmuelling, G.; Placke, T.; Kloepsch, R.; Fromm, O.; Meyer, H.W.; Passerini, S.; Winter, M. X-ray diffraction studies of the electrochemical intercalation of bis(trifluoromethanesulfonyl)imide anions into graphite for dual-ion cells. *J. Power Sources* **2013**, *239*, 563–571. [CrossRef]
48. Xu, J.H.; Turney, D.E.; Jadhav, A.L.; Messinger, R.J. Effects of Graphite Structure and Ion Transport on the Electrochemical Properties of Rechargeable Aluminum-Graphite Batteries. *ACS Appl. Energy Mater.* **2019**, *11*, 7799–7810. [CrossRef]
49. Sonia, F.J.; Jangid, M.K.; Ananthoju, B.; Aslam, M.; Johari, P.; Mukhopadhyay, A. Understanding the Li-storage in few layers graphene with respect to bulk graphite: Experimental, analytical and computational study. *J. Mater. Chem. A* **2017**, *5*, 8662–8679. [CrossRef]
50. Sonia, F.J.; Jangid, M.K.; Aslam, M.; Johari, P.; Mukhopadhyay, A. Enhanced and faster potassium storage in graphene with respect to graphite: A comparative study with lithium storage. *ACS Nano* **2019**, *13*, 2190–2204. [CrossRef]
51. Zhang, E.; Cao, W.; Wang, B.; Yu, X.; Wang, L.; Xu, Z.; Lu, B. A novel aluminum dual-ion battery. *Energy Storage Mater.* **2018**, *11*, 91–99. [CrossRef]
52. Son, D.K.; Kim, J.; Raj, M.R.; Lee, G. Elucidating the structural redox behaviors of nanostructured expanded graphite anodes toward fast-charging and high-performance lithium-ion batteries. *Carbon N. Y.* **2021**, *175*, 187–201. [CrossRef]
53. Skaltsas, T.; Ke, X.; Bittencourt, C.; Tagmatarchis, N. Ultrasonication induces oxygenated species and defects onto exfoliated graphene. *J. Phys. Chem. C* **2013**, *117*, 23272–23278. [CrossRef]
54. Shibaev, A.A.; Mal'tsev, L.I.; Petrov, V.M.; Maksimovskii, E.A.; Ukhina, A.V.; Prosanov, I.Y.; Popov, M.V.; Bannov, A.G. Studies of ultrasonication of exfoliated graphite. *Prot. Met. Phys. Chem. Surf.* **2017**, *53*, 261–267. [CrossRef]
55. Xu, J.H.; Schoetz, T.; McManus, J.R.; Subramanian, V.R.; Fields, P.W.; Messinger, R.J. Tunable Pseudocapacitive Intercalation of Chloroaluminate Anions into Graphite Electrodes for Rechargeable Aluminum Batteries. *J. Electrochem. Soc.* **2021**, *168*, 060514. [CrossRef]
56. Liu, C.; Liu, Z.; Li, Q.; Niu, H.; Wang, C.; Wang, Z.; Gao, B. Binder-free ultrasonicated graphite flakes@carbon fiber cloth cathode for rechargeable aluminum-ion battery. *J. Power Sources* **2019**, *438*, 226950. [CrossRef]
57. Kim, J.; Raj, M.R.; Lee, G. High-Defect-Density Graphite for Superior-Performance Aluminum-Ion Batteries with Ultra-Fast Charging and Stable Long Life. *Nano-Micro Lett.* **2021**, *13*, 171. [CrossRef]

58. Peng, Y.; Chen, Z.; Zhang, R.; Zhou, W.; Gao, P.; Wu, J.; Liu, H.; Liu, J.; Hu, A.; Chen, X. Oxygen-Containing Functional Groups Regulating the Carbon/Electrolyte Interfacial Properties Toward Enhanced K+ Storage. *Nano-Micro Lett.* **2021**, *13*, 192. [CrossRef]

59. Xiong, D.; Li, X.; Shan, H.; Zhao, Y.; Dong, L.; Xu, H.; Zhang, X.; Li, D.; Sun, X. Oxygen-containing Functional Groups Enhancing Electrochemical Performance of Porous Reduced Graphene Oxide Cathode in Lithium Ion Batteries. *Electrochim. Acta* **2015**, *174*, 762–769. [CrossRef]

60. Cao, H.; Peng, X.; Zhao, M.; Liu, P.; Xu, B.; Guo, J. Oxygen functional groups improve the energy storage performances of graphene electrochemical supercapacitors. *RSC Adv.* **2018**, *8*, 2858–2865. [CrossRef]

61. Tian, S.; Qi, L.; Wang, H. Difluoro(oxalato)borate anion intercalation into graphite electrode from ethylene carbonate. *Solid State Ionics* **2016**, *291*, 42–46. [CrossRef]

62. Lin, M.C.; Gong, M.; Lu, B.; Wu, Y.; Wang, D.Y.; Guan, M.; Angell, M.; Chen, C.; Yang, J.; Hwang, B.J.; et al. An ultrafast rechargeable aluminium-ion battery. *Nature* **2015**, *520*, 325–328. [CrossRef] [PubMed]

63. Flores, E.; Novák, P.; Berg, E.J. In situ and Operando Raman spectroscopy of layered transition metal oxides for Li-ion battery cathodes. *Front. Energy Res.* **2018**, *6*, 82. [CrossRef]

64. Wang, D.Y.; Wei, C.Y.; Lin, M.C.; Pan, C.J.; Chou, H.L.; Chen, H.A.; Gong, M.; Wu, Y.; Yuan, C.; Angell, M.; et al. Advanced rechargeable aluminium ion battery with a high-quality natural graphite cathode. *Nat. Commun.* **2017**, *8*, 14283. [CrossRef]

65. Julien, C.M.; Mauger, A. In situ Raman analyses of electrode materials for Li-ion batter. *AIMS Mater. Sci.* **2018**, *5*, 650–698. [CrossRef]

66. Liang, H.J.; Hou, B.H.; Li, W.H.; Ning, Q.L.; Yang, X.Y.; Gu, Z.Y.; Nie, X.J.; Wang, G.; Wu, X.L. Staging Na/K-ion de-/intercalation of graphite retrieved from spent Li-ion batteries: In operando X-ray diffraction studies and an advanced anode material for Na/K-ion batteries. *Energy Environ. Sci.* **2019**, *12*, 3575–3584. [CrossRef]

67. Pan, C.J.; Yuan, C.; Zhu, G.; Zhang, Q.; Huang, C.J.; Lin, M.C.; Angell, M.; Hwang, B.J.; Kaghazchi, P.; Dai, H. An operando X-ray diffraction study of chloroaluminate anion-graphite intercalation in aluminum batteries. *Proc. Natl. Acad. Sci. USA* **2018**, *115*, 5670–5675. [CrossRef]

68. Wang, H.; Bai, Y.; Chen, S.; Luo, X.; Wu, C.; Wu, F.; Lu, J.; Amine, K. Binder-free V_2O_5 cathode for greener rechargeable aluminum battery. *ACS Appl. Mater. Interfaces* **2015**, *7*, 80–84. [CrossRef]

69. Sheet, D.; Bera, A.; Fu, Y.; Desmecht, A.; Riant, O.; Hermans, S. Carbon-Nanotube-Appended PAMAM Dendrimers Bearing Iron(II) α-Keto Acid Complexes: Catalytic Non-Heme Oxygenase Models. *Chem.—A Eur. J.* **2019**, *25*, 9191–9196. [CrossRef]

70. Takehira, H.; Karim, M.R.; Shudo, Y.; Fukuda, M.; Mashimo, T.; Hayami, S. Modulating the Work Function of Graphene by Pulsed Plasma Aided Controlled Chlorination. *Sci. Rep.* **2018**, *8*, 17392. [CrossRef]

71. Jagadeesh, M.S.; Bussetti, G.; Calloni, A.; Yivlialin, R.; Brambilla, L.; Accogli, A.; Gibertini, E.; Alliata, D.; Goletti, C.; Ciccacci, F.; et al. Incipient Anion Intercalation of Highly Oriented Pyrolytic Graphite Close to the Oxygen Evolution Potential: A Combined X-ray Photoemission and Raman Spectroscopy Study. *J. Phys. Chem. C* **2019**, *123*, 1790–1797. [CrossRef]

72. Schnyder, B.; Alliata, D.; Kötz, R.; Siegenthaler, H. Electrochemical intercalation of perchlorate ions in HOPG: An SFM/LFM and XPS study. *Appl. Surf. Sci.* **2001**, *173*, 221–232. [CrossRef]

73. Zou, L.; Huang, B.; Huang, Y.; Huang, Q.; Wang, C. An investigation of heterogeneity of the degree of graphitization in carbon–carbon composites. *Mater. Chem. Phys.* **2003**, *82*, 654–662. [CrossRef]

74. Warren, B.E. X-ray Diffraction in Random Layer Lattices. *Phys. Rev.* **1941**, *59*, 693–698. [CrossRef]

75. Cançado, L.G.; Takai, K.; Enoki, T.; Endo, M.; Kim, Y.A.; Mizusaki, H.; Jorio, A.; Coelho, L.N.; Magalhães-Paniago, R.; Pimenta, M.A. General equation for the determination of the crystallite size La of nanographite by Raman spectroscopy. *Appl. Phys. Lett.* **2006**, *88*, 163106. [CrossRef]

76. Jayaramulu, K.; Dubal, D.; Nagar, B.; Ranc, V.; Tomanec, O.; Petr, M.; Datta, K.K.R.; Zboril, R.; Gómez-Romero, P.; Fischer, R.A. Ultrathin Hierarchical Porous Carbon Nanosheets for High-Performance Supercapacitors and Redox Electrolyte Energy Storage. *Adv. Mater.* **2018**, *30*, e1705789. [CrossRef]

77. Pei, S.; Cheng, H.M. The reduction of graphene oxide. *Carbon N. Y.* **2012**, *50*, 3210–3228. [CrossRef]

78. Stobinski, L.; Lesiak, B.; Malolepszy, A.; Mazurkiewicz, M.; Mierzwa, B.; Zemek, J.; Jiricek, P.; Bieloshapka, I. Graphene oxide and reduced graphene oxide studied by the XRD, TEM and electron spectroscopy methods. *J. Electron Spectrosc. Relat. Phenom.* **2014**, *195*, 145–154. [CrossRef]

79. Yang, D.; Velamakanni, A.; Bozoklu, G.; Park, S.; Stoller, M.; Piner, R.D.; Stankovich, S.; Jung, I.; Field, D.A.; Ventrice, C.A., Jr.; et al. Chemical analysis of graphene oxide films after heat and chemical treatments by X-ray photoelectron and Micro-Raman spectroscopy. *Carbon N. Y.* **2009**, *47*, 145–152. [CrossRef]

80. Fan, L.-Z.; Liu, J.-L.; Ud-Din, R.; Yan, X.; Qu, X. The effect of reduction time on the surface functional groups and supercapacitive performance of graphene nanosheets. *Carbon* **2012**, *50*, 3724–3730. [CrossRef]

81. Yoshida, A.; Tanahashi, I.; Nishino, A. Effect of concentration of surface acidic functional groups on electric double-layer properties of activated carbon fibers. *Carbon* **1990**, *28*, 611–615. [CrossRef]

82. Bokare, A.; Nordlund, D.; Melendrez, C.; Robinson, R.; Keles, O.; Wolcott, A.; Erogbogbo, F. Surface functionality and formation mechanisms of carbon and graphene quantum dots. *Diam. Relat. Mater.* **2020**, *110*, 108101. [CrossRef]